J. Fluid Mech. (2025), *vol.* 1014, A30, doi:10.1017/jfm.2025.10318

Attenuation mechanism of wall-bounded turbulence by heavy finite-size particles

Yutaro Motoori[1] and **Susumu Goto**[1]

[1]Graduate School of Engineering Science, The University of Osaka, 1-3 Machikaneyama, Toyonaka, Osaka 560-8531, Japan

Corresponding authors: Yutaro Motoori, y.motoori.es@osaka-u.ac.jp; Susumu Goto, s.goto.es@osaka-u.ac.jp

(Received 2 October 2024; revised 10 April 2025; accepted 26 May 2025)

To elucidate the attenuation mechanism of wall-bounded turbulence due to heavy small particles, we conduct direct numerical simulations (DNS) of turbulent channel flow laden with finite-size solid particles. When particles cannot follow the swirling motions of wall-attached vortices, vortex rings are created around the particles. These particle-induced vortices lead to additional energy dissipation, reducing the turbulent energy production from the mean flow. This mechanism results in the attenuation of turbulent kinetic energy, which is more significant when the Stokes number of particles is larger or particle size is smaller under the condition that the volume fraction of particles is fixed. Moreover, we propose a method to quantitatively predict the degree of turbulence attenuation without using DNS data by estimating the additional energy dissipation rate in terms of particle properties.

Key words: turbulent flows, particle/fluid flow

1. Introduction

The addition of small particles can attenuate turbulence. This phenomenon has been demonstrated by many experiments since the last century. For example, Gore & Crowe (1989) compiled experimental results on turbulence modulation, demonstrating that when the particle diameter is about 0.1 times smaller than the integral length of turbulence, the particles can attenuate turbulence; otherwise, the larger particles enhance it. Although many authors (Hosokawa & Tomiyama 2004; Righetti & Romano 2004; Tanaka & Eaton 2008; Noguchi & Nezu 2009; Yu *et al.* 2021) proposed other parameters that characterise turbulence modulation, there is a consensus, supported by experiments (Maeda, Hishida

& Furutani 1980; Tsuji, Morikawa & Shiomi 1984; Rogers & Eaton 1991; Kulick, Fessler & Eaton 1994; Fessler & Eaton 1999; Kussin & Sommerfeld 2002; Yang & Shy 2005) and direct numerical simulations (DNS) (Ferrante & Elghobashi 2003; ten Cate *et al.* 2004; Vreman 2007; Zhao, Andersson & Gillissen 2010; Abdelsamie & Lee 2012; Zhao, Andersson & Gillissen 2013; Li, Luo & Fan 2016; Liu *et al.* 2017; Mortimer, Njobuenwu & Fairweather 2019; Oka & Goto 2022; Peng, Sun & Wang 2023), that small heavy particles can lead to turbulence attenuation.

In addition to these studies, to accumulate a significant body of knowledge on turbulence modulation due to particles, many researchers (ten Cate *et al.* 2004; Burton & Eaton 2005; Lucci, Ferrante & Elghobashi 2010; Yeo *et al.* 2010; Bellani *et al.* 2012; Wang *et al.* 2014; Schneiders, Meinke & Schröder 2017; Uhlmann & Chouippe 2017; Oka & Goto 2022; Shen *et al.* 2022; Peng *et al.* 2023) conducted DNS of turbulence interacting with finite-size spherical particles in a periodic box. Among these studies, it is crucial to highlight the observation reported by ten Cate *et al.* (2004) that the energy dissipation rate produced by the relative motion between particles and fluid is a key quantity for significant attenuation of turbulent kinetic energy. In addition to their study, many authors (Squires & Eaton 1990; Elghobashi 1994; Kulick *et al.* 1994; Paris 2001; Hwang & Eaton 2006; Mandø *et al.* 2009; Balachandar & Eaton 2010; Yeo *et al.* 2010; Wang *et al.* 2014; Peng, Ayala & Wang 2019*b*) also emphasised the importance of the additional energy dissipation rate for turbulence attenuation. Recently, our group (Oka & Goto 2022) conducted DNS of periodic turbulence laden with finite-size particles and derived a formula to describe the turbulence attenuation rate. This formula is based on the physical picture of the turbulence attenuation that the additional energy dissipation due to particles bypasses the energy cascade. Balachandar, Peng & Wang (2024) further developed this view to model the energy balance between particles and turbulence at subgrid scales. Thus, the additional energy dissipation due to particles is crucial for turbulence attenuation. However, most of these results were obtained through numerical analyses of periodic turbulence without walls, although the pioneering studies on turbulence modulation by particles were made using experiments of air turbulence bounded by solid walls (Tsuji & Morikawa 1982; Tsuji *et al.* 1984; Kulick *et al.* 1994). Therefore, the next important issue is understanding the modulation mechanism of wall-bounded turbulence. This is the target of the present study.

Kulick *et al.* (1994) experimentally demonstrated for turbulent channel flow that heavy copper particles attenuated turbulence intensity more effectively than glass particles. They concluded that as the relaxation time τ_p of particles becomes longer than the time scale τ_f of fluid motion, i.e. as the Stokes number $St = \tau_p/\tau_f$ increases, the degree of turbulence attenuation becomes more significant. Note that the relaxation time is longer for heavier particles if they have the same diameter. Similarly to turbulence in a periodic box, the attenuation of wall-bounded turbulence for large St is also explained by a relative velocity between particles and fluid because it leads to significant energy dissipation around particles (Paris 2001; Peng *et al.* 2019*a*). To understand the modulation mechanism of wall-bounded turbulence, many DNS studies were conducted for turbulent channel flow laden with heavy pointwise particles (Dritselis & Vlachos 2008, 2011; Lee, Ahn & Sung 2015; Wang & Richter 2019; Zhou *et al.* 2020) and finite-size ones (Kajishima *et al.* 2001; Uhlmann 2008; Zeng *et al.* 2008; Shao, Wu & Yu 2012; Fornari *et al.* 2016; Li *et al.* 2016; Yu *et al.* 2017; Peng *et al.* 2019*a*,*b*; Costa, Brandt & Picano 2020; Muramulla *et al.* 2020; Costa, Brandt & Picano 2021; Xia *et al.* 2021; Yu *et al.* 2021; Brandt & Coletti 2022; Shen *et al.* 2024). For example, Zhao *et al.* (2013) and Yu *et al.* (2021) discussed interactions between particles and turbulence on the basis of turbulent kinetic energy and Reynolds stress budgets. Peng *et al.* (2019*b*) depicted a schematic of turbulence modulation in the viscous sublayer and the buffer layer. Recently, Shen *et al.* (2024) investigated particle parameter dependence of turbulence modulation especially in the near-wall region. However, a framework for predicting the degree of attenuation is incomplete because we do not fully understand the concrete picture of the attenuation mechanism in wall-bounded turbulence.

The purposes of the present study are (i) to understand the attenuation mechanism of wall-bounded turbulence by small heavy particles and (ii) to predict the degree of turbulence attenuation in terms of particle properties. For these purposes, we conduct DNS of turbulent channel flow with finite-size spherical particles, systematically changing the particle diameter, mass density and turbulence Reynolds number. In particular, we focus on heavy particles as small as the buffer-layer coherent structures. To investigate the interaction between particles and turbulence, we assume that the gravitational effects are negligible.

In the following, we first describe the coupled DNS method for turbulent channel flow with particles (§ 2). Then, we examine the modulation of coherent vortices in real space (§ 3.1) and quantitatively investigate the modulation of the energy transfer mechanism (§§ 3.2–3.4). Then, based on this attenuation mechanism, we develop an argument to predict the degree of turbulence attenuation (§ 4).

2. Methods

2.1. *Direct numerical simulations*

We numerically simulate turbulence laden with finite-size particles between two parallel planes. Under non-slip boundary conditions on the surfaces of the particles and walls, the flow obeys the Navier–Stokes equation,

$$\frac{\partial \boldsymbol{u}}{\partial t} + (\boldsymbol{u} \cdot \nabla)\boldsymbol{u} = \nabla \cdot \mathsf{T} + \boldsymbol{f}^{ex}, \tag{2.1}$$

and the continuity equation,

$$\nabla \cdot \boldsymbol{u} = 0, \tag{2.2}$$

where $\boldsymbol{u}(\boldsymbol{x}, t)$ and $p(\boldsymbol{x}, t)$ are the fluid velocity and the pressure at position $\boldsymbol{x}$ and time t, respectively. In (2.1), T is the stress tensor divided by the mass density for a Newtonian fluid and $\boldsymbol{f}^{ex}$ $(= (f_x^{ex}, 0, 0))$ is the force due to a constant pressure difference. We solve these equations using the immersed boundary method (IBM) proposed by Breugem (2012). In this method, similarly to the original method by Uhlmann (2005), we introduce a force between particles and fluid. More concretely, instead of solving (2.1) under the boundary conditions on the particle surfaces, we solve

$$\frac{\partial \boldsymbol{u}}{\partial t} + (\boldsymbol{u} \cdot \nabla)\boldsymbol{u} = -\frac{1}{\rho_f}\nabla p + \nu \nabla^2 \boldsymbol{u} + \boldsymbol{f}^{ex} + \boldsymbol{f}^{IBM} \tag{2.3}$$

in the entire computational domain including the inside of particles. Here, ρ_f and ν denote the fluid mass density and kinematic viscosity, respectively, and $\boldsymbol{f}^{IBM}$ is the force per unit mass to satisfy the non-slip boundary condition at the Lagrangian points distributed on the surface of each particle.

We consider the motion of spherical solid particles with a mass density ρ_p, volume V_p and moment of inertia I_p. The equations of motion of a particle with velocity $\boldsymbol{u}_p(t) = \mathrm{d}\boldsymbol{x}_p/\mathrm{d}t$ and angular velocity $\boldsymbol{\omega}_p(t)$ are

$$\rho_p V_p \frac{\mathrm{d}\boldsymbol{u}_p}{\mathrm{d}t} = \oint_{\partial V_p} \mathsf{T} \cdot \boldsymbol{n}^{\textcircled{p}}\, \mathrm{d}S + \rho_f V_p \boldsymbol{f}^{ex} + \boldsymbol{F}^{\leftrightarrow p} \tag{2.4}$$

and

$$I_p \frac{\mathrm{d}\boldsymbol{\omega}_p}{\mathrm{d}t} = \oint_{\partial V_p} \boldsymbol{r} \times (\mathbf{T} \cdot \boldsymbol{n}^{ⓟ})\, \mathrm{d}S + \boldsymbol{T}^{\leftrightarrow p}. \tag{2.5}$$

Here, $\boldsymbol{n}^{ⓟ}$ denotes the outward-pointing normal vector on the surface ∂V_p of the particle, $\boldsymbol{r}$ is the position vector relative to the particle centre and $\boldsymbol{F}^{\leftrightarrow p}$ and $\boldsymbol{T}^{\leftrightarrow p}$ are the force and torque acting on the particle due to collisions with other particles or solid walls, respectively. In the IBM, we evaluate the first term of the right-hand side of (2.4) with

$$\oint_{\partial V_p} \mathbf{T} \cdot \boldsymbol{n}^{ⓟ}\, \mathrm{d}S = -\rho_f \sum_{\ell=1}^{N_\ell} \boldsymbol{f}_\ell^{IBM}\, \Delta V_\ell + \rho_f \frac{\mathrm{d}}{\mathrm{d}t} \int_{V_p} \boldsymbol{u}\, \mathrm{d}V - \rho_f V_p \boldsymbol{f}^{ex}. \tag{2.6}$$

Here, $\boldsymbol{f}_\ell^{IBM}$ is the fluid force (per unit mass) by particles acting at the N_ℓ Lagrangian points distributed on the particle surface and ΔV_ℓ is the volume of a Lagrangian grid cell. The first term of the right-hand side of (2.5) is given by $\boldsymbol{r}\times$ (2.6). Then, we evaluate the last terms ($\boldsymbol{F}^{\leftrightarrow p}$ and $\boldsymbol{T}^{\leftrightarrow p}$) using an elastic model (Glowinski *et al.* 2001) for the normal component of the contact force. We neglect the frictional force and collision torque.

To couple flow and particle motion, we alternately integrate their governing equations with the second-order Crank–Nicolson method for the viscous term of the fluid and explicit third-order low-storage three-step Runge–Kutta method for the other terms. Details of the numerical method are as described in Breugem (2012).

2.2. *Parameters*

We simulate turbulent channel flow at four values of the friction Reynolds number: $Re_\tau = u_\tau h/\nu = 512$, 360, 256 and 180, where u_τ is the friction velocity and h is the channel half-width. Note that since the external driving force f_x^{ex} is constant, the frictional force acting on the wall and therefore Re_τ are kept constant even in the case with particles. The computational domain sides are $4h$, $2h$ and $2h$ in the streamwise x, wall-normal y and spanwise z directions, respectively. The grid width is $\varDelta^+ = 2$ for all directions. Here, $\cdot^+$ denotes a quantity normalised by u_τ and ν.

We add particles into turbulence in a statistically steady state. The particles are characterised by three parameters related to the diameter D, mass density ρ_p and the number N_p of particles. Fixing the volume fraction $\varLambda_0\ (= N_p V_p/(16h^3))$ at 0.0082, we change the other two parameters: D and ρ_p. The particle diameters are $D^+ = 16$, 32 and 64 for $Re_\tau = 512$; $D^+ = 16$ and 32 for $Re_\tau = 360$ and 256; and $D^+ = 16$ for $Re_\tau = 180$. We list in table 1 the parameters of particles. The particle diameters are comparable to or a few times larger than the diameter of tubular quasi-streamwise vortices in the buffer layer; but they are sufficiently smaller than the channel half-width (i.e. $D/h \lesssim 0.1$). All particles are resolved to satisfy $D/\Delta \geqslant 8$, which is the same as in our previous studies (Oka & Goto 2022; Awai, Motoori & Goto 2025). For the mass density ρ_p, we set it to be larger than that ρ_f of the fluid: $\rho_p/\rho_f = 2$, 8, 32 and 128. We neglect gravitational effects. In this situation, we observe only turbulence attenuation because the relative velocity between particles and fluid is not enough to enhance turbulence. This is consistent with an indicator for turbulence enhancement proposed by Yu *et al.* (2021); see Appendix A. In addition, we also recently discussed turbulence enhancement in channel flow with gravity (Motoori & Goto 2025).

In the following, we show results for turbulence modulation using the relaxation time τ_p of particles to the fluid motion instead of ρ_p/ρ_f. Here, we define the relaxation time as $\tau_p = \rho_p D^2/(18\rho_f \nu)$ by assuming Stokes drag. We list in table 1 the values of $St_+ = \tau_p/\tau^+$, defined with the wall friction time $\tau^+\ (= \nu/u_\tau^2)$, and $St_h = \tau_p/\tau_h$, defined

Re_τ	D^+	D/h	D/Δ	ρ_p/ρ_f	St_+	St_h	N_p
512	16	0.031	8	2	28	0.056	8192
512	16	0.031	8	8	114	0.22	8192
512	16	0.031	8	32	455	0.89	8192
512	16	0.031	8	128	1820	3.6	8192
512	32	0.063	16	2	114	0.22	1024
512	32	0.063	16	8	455	0.89	1024
512	32	0.063	16	32	1820	3.6	1024
512	32	0.063	16	128	7282	14	1024
512	64	0.13	32	2	455	0.89	128
512	64	0.13	32	8	1820	3.6	128
512	64	0.13	32	32	7282	14	128
512	64	0.13	32	128	29127	57	128
360	16	0.044	8	2	28	0.078	2847
360	16	0.044	8	8	114	0.32	2847
360	16	0.044	8	32	455	1.3	2847
360	16	0.044	8	128	1820	5.1	2847
360	32	0.089	16	2	114	0.32	356
360	32	0.089	16	8	455	1.3	356
360	32	0.089	16	32	1820	5.1	356
360	32	0.089	16	128	7282	20	356
256	16	0.063	8	2	28	0.11	1024
256	16	0.063	8	8	114	0.44	1024
256	16	0.063	8	32	455	1.8	1024
256	16	0.063	8	128	1820	7.1	1024
256	32	0.13	16	2	114	0.44	128
256	32	0.13	16	8	455	1.8	128
256	32	0.13	16	32	1820	7.1	128
256	32	0.13	16	128	7282	28	128
180	16	0.089	8	2	28	0.16	356
180	16	0.089	8	8	114	0.63	356
180	16	0.089	8	32	455	2.5	356
180	16	0.089	8	128	1820	10	356

Table 1. Particle parameters.

with the largest eddy turnover time $\tau_h = h/u_\tau$. The examined particles have relaxation time τ_p in a wide range between the swirling time scales of the smallest and largest vortices. Specifically, the shortest relaxation time ($St_+ = 28$) is comparable to the time scale of coherent structures in the buffer layer (Soldati & Marchioli 2009). In other words, none of the simulated particles can thoroughly follow the swirl of streamwise vortices in the buffer layer. On the other hand, St_h ($= St_+ Re_\tau$) represents particles' ability to follow the largest vortices, that is, the wall-attached vortices in the outer layer. Particles with $St_h \lesssim 1$ can follow the swirling motions of the outer-layer vortices, whereas those with $St_h \gtrsim 1$ cannot follow them.

2.3. *Validation*

Before showing results in the next section, we validate our DNS by simulating particle-laden turbulence in the same system as investigated by Yu *et al.* (2021). For this, we impose a time-dependent pressure gradient to maintain a constant flow rate and apply the gravitational force to ensure that the ratio between the characteristic settling velocity u_g

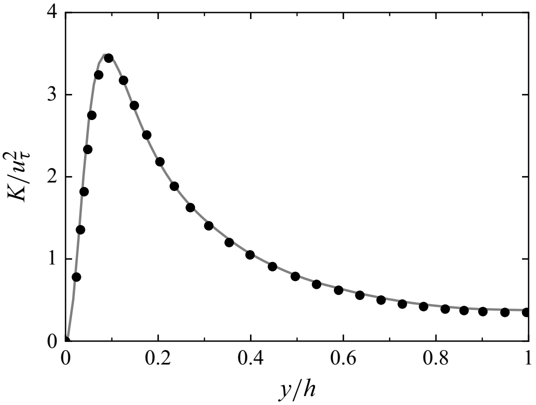

Figure 1. Wall-normal profiles of the mean turbulent kinetic energy $K(y)$. The circles show the result by Yu *et al.* (2021). The parameters are $D/h = 0.1$, $\rho_p/\rho_f = 2$, $\Lambda_0 = 0.0236$, $u_g/U_b = 0.159$ and $U_b(2h)/\nu = 5746$. Data are extracted from figure 8(*a*) of their paper. The curve shows the present DNS result with the same parameters.

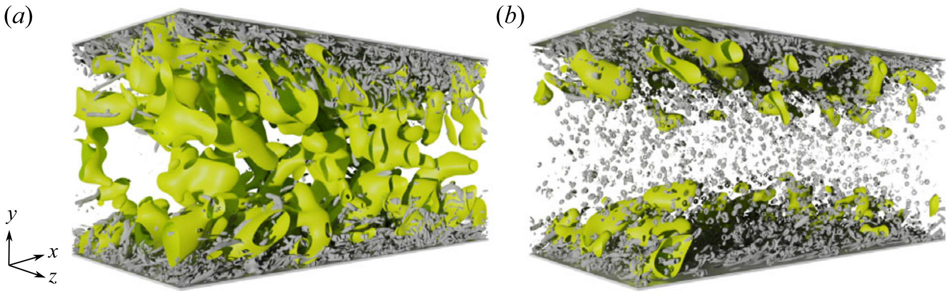

Figure 2. Visualisation of coherent vortices in turbulence at $Re_\tau = 512$ laden with particles with the same diameter ($D/h = 0.031$, i.e. $D^+ = 16$) but different values of the Stokes number: (*a*) $St_h = 0.056$ and (*b*) 3.6. Grey vortices are identified by positive isosurfaces of the second invariant Q of the velocity gradient tensor. Yellow vortices are identified by the second invariant $\widetilde{Q}^{(\ell)}$ of the velocity gradient tensor coarse-grained at $\ell = 0.2h$. We set the thresholds as $Q^+ = 7.0 \times 10^{-3}$ and $\widetilde{Q}^{(\ell)+} = 3.0 \times 10^{-5}$.

($= \sqrt{4D(\rho_p/\rho_f - 1)g/3}$, with g being the magnitude of the gravitational acceleration) of particles and the mean bulk velocity U_b is 0.159. Figure 1 shows the wall-normal profiles of the mean turbulent kinetic energy,

$$K(y) = \frac{1}{2}\overline{|\boldsymbol{u}'(\boldsymbol{x}, t)|^2}, \tag{2.7}$$

in the statistically steady state. Here, $\overline{\cdot}$ denotes the average in the streamwise and spanwise directions and time over the fluid region outside particles, and $\boldsymbol{u}'(\boldsymbol{x}, t)$ ($= \boldsymbol{u}(\boldsymbol{x}, t) - \boldsymbol{U}(y)$) is the fluctuation fluid velocity, where $\boldsymbol{U}(y)$ ($= \overline{\boldsymbol{u}(\boldsymbol{x}, t)}$) is the mean velocity. We can confirm that our results are in good agreement with those of Yu *et al.* (2021). In the following analyses, we discuss the statistically steady state after adding the particles.

3. Attenuation mechanism

3.1. *Modulation of coherent vortices*

First, let us examine the modulation of coherent vortices in turbulence. Figure 2 shows vortices in turbulence at $Re_\tau = 512$ laden with the smallest ($D/h = 0.031$, i.e. $D^+ = 16$)

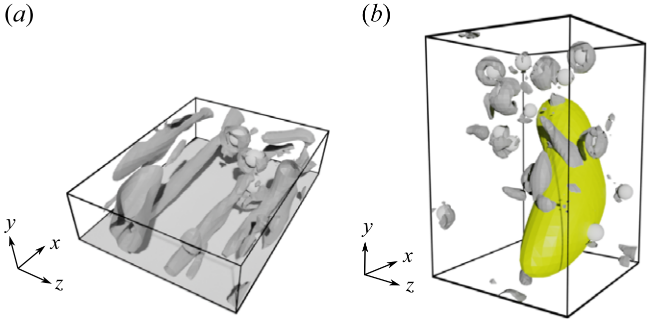

Figure 3. Magnification of subdomains in figure 2(*b*) for (*a*) $0 \leqslant y^+ \leqslant 50$ and (*b*) $0.3 \leqslant y/h \leqslant 0.75$ (i.e. $154 \leqslant y^+ \leqslant 384$). Particles are depicted by white spheres.

particles. The Stokes number differs between the panels: $St_h = 0.056$ (figure 2*a*) and 3.6 (figure 2*b*). We show vortices at two different scales: the grey objects are the smallest vortices identified by positive isosurfaces of the second invariant Q of the velocity gradient tensor. To extract channel-half-width-scale vortices (i.e. wall-attached vortices in the outer layer), we apply the three-dimensional Gaussian filter (Motoori & Goto 2019) with filter width $\ell = 0.2h$ to the fluctuation velocity. We then evaluate the second invariant $\widetilde{Q}^{(\ell)}$ of the coarse-grained velocity gradient tensor and show its positive isosurfaces in yellow. It is evident in figure 2(*a*) that the yellow outer-layer vortices are developed even in the presence of particles with smaller St_h $(= 0.056)$; whereas, in figure 2(*b*), these vortices are almost entirely attenuated due to particles with larger St_h $(= 3.6)$.

It is also important to observe in figure 2(*b*) that vortex rings are attached to particles. Figures 3(*a*) and 3(*b*) are the magnifications of subdomains in figure 2(*b*) in the buffer and outer layers, respectively. Here, particles are depicted by white spheres. There are many vortex rings around particles in the both layers. Since St_h of these particles is larger than 1, they can follow neither the outer-layer vortices (with the longest time scale in the turbulence) nor the buffer-layer vortices. The particles also cannot follow the mean flow because its time scale is comparable to the turnover time of the wall-attached vortices at each height. This explains the reason why these vortex rings are perpendicular to the streamwise direction. If the particle Reynolds number were higher, the vortex rings would be shed from the particles. In contrast, for $St_h \ll 1$ (see figure 2*a*), there are no vortex rings in the outer layer. These results therefore imply that the presence of particle-induced vortices results in the reduction of turbulent vortices. As is discussed in detail in the following (see § 3.4), these small vortices induced by particles are indeed important because they produce the additional energy dissipation, which is relevant to the turbulence attenuation.

3.2. *Turbulent kinetic energy*

To quantify the degree of turbulence modulation at each height, we evaluate the mean turbulent kinetic energy $K(y)$ defined as (2.7). As mentioned below (2.7), when we take the spatial average, we only take into account the fluid region outside particles. Figure 4 shows the wall-normal profiles of $K(y)$ for turbulence at $Re_\tau = 512$. The blue dashed line indicates the value $K_\times$ in the single-phase flow, where the subscript $_\times$ denotes the value in the single-phase flow. First, let us look at figure 4(*a*), which shows the St_h dependence for the smallest $(D/h = 0.031)$ particles. Lighter and thicker lines indicate results for larger St_h. We see that, irrespective of the height, turbulent kinetic energy is attenuated more significantly for larger St_h. This is consistent with the observation in figure 2 that particles with larger St_h more significantly attenuate outer-layer energetic vortices.

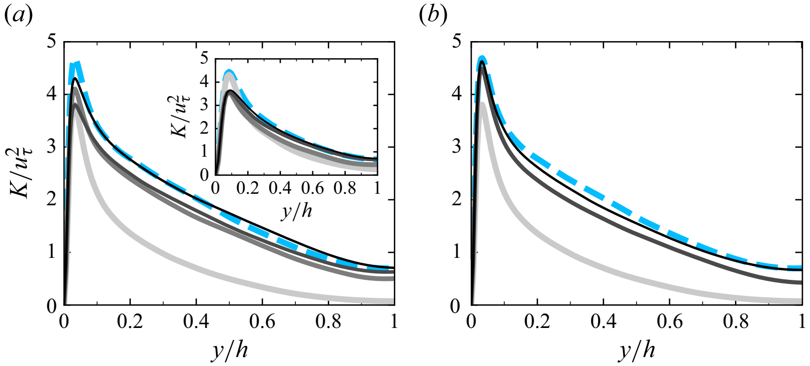

Figure 4. Wall-normal profiles of the mean turbulent kinetic energy $K(y)$ (2.7) at $Re_\tau = 512$. (*a*) The Stokes-number dependence ($St_h = 0.056$ (black), 0.22 (dark grey), 0.89 (light grey) and 3.6 (very light grey)) for the common particle diameter $D/h = 0.031$. (*b*) The particle-diameter dependence ($D/h = 0.13$ (black), 0.063 (grey) and 0.031 (light grey)) for the common Stokes number $St_h = 3.6$. The blue dashed line shows the result for the single-phase flow. The inset in (*a*) shows the results for $Re_\tau = 180$ with $St_h = 0.016$ (black), 0.63 (dark grey), 2.5 (light grey) and 10 (very light grey).

More precisely, we can observe in figure 4(*a*) that as St_h increases, K is attenuated from a lower height. For example, particles with $St_h = 0.056$, that is, $St_+ = 28$ (the darkest and thinnest line), attenuate turbulence only for $y/h \lesssim 0.1$ (i.e. $y^+ \lesssim 50$). This is because the particle relaxation time is too long for them to follow the swirls of the buffer-layer vortices (whose time scale is of the order of $10\tau_+$) but short enough to follow the larger wall-attached vortices such as the outer-layer vortices (because $St_h \ll 1$). For the other Re_τ, we have also confirmed that particles with $St_+ = 28$ attenuate turbulent kinetic energy only in the buffer layer (figures omitted). In contrast, particles with $St_h = 3.6$ (the lightest line) attenuate the turbulent kinetic energy at any height. We observe similar trends with respect to St_h for $Re_\tau = 180$ (see the inset in figure 4*a*) and for the results of smaller particles ($D^+ \approx 10$) in Shen *et al.* (2024).

Figure 4(*b*) shows results for common $St_h = 3.6$ but different values of D/h (darker and thinner lines indicate larger particles). Since St_h of these particles is larger than 1, they attenuate turbulence at all heights. It is, however, important to see in this panel that the attenuation rate depends on the particle size; more precisely, it is larger for smaller diameters for a fixed volume fraction of particles.

Thus, when particles cannot follow the wall-attached vortices (and therefore the mean flow) at a given height y, the turbulent kinetic energy around y is attenuated. The degree of the turbulence attenuation is larger for larger Stokes numbers (figure 4*a*) and smaller diameters (figure 4*b*).

Next, we consider spatially averaged quantities. Figure 5 shows the average attenuation rate,

$$\mathcal{A} = 1 - \frac{\langle K \rangle}{\langle K_\times \rangle}, \tag{3.1}$$

of turbulent kinetic energy as a function of St_h. Here, $\langle \cdot \rangle$ denotes the spatial average over the fluid region outside the particles. Lighter colours indicate smaller D/h and different symbols represent different values of Re_τ. We can see that irrespective of Re_τ, the average attenuation rate gets larger for larger St_h and smaller D/h.

To explain these behaviours, we investigate how the kinetic energy transfers from the mean flow to turbulence. Turbulent kinetic energy $K(y)$ at a given height y increases due to the production by the mean flow, transport from other heights and work done by

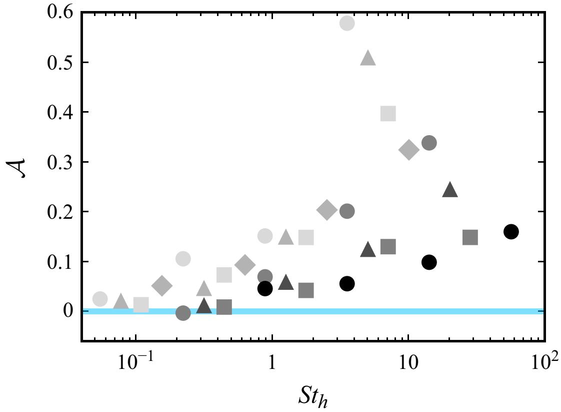

Figure 5. Average attenuation rate $\mathcal{A}$ (3.1) of turbulent kinetic energy as a function of St_h. Different symbols show the results for $Re_\tau = 512$ (circles), 360 (triangles), 256 (squares) and 180 (diamonds). The colour indicates D/h (lighter symbols indicate smaller particles).

particles; on the other hand, it decreases due to transport to other heights and dissipation into heat. Since the average of the spatial transport over the entire channel vanishes, the average budget of turbulent kinetic energy $\langle K \rangle$ reads

$$\langle \mathcal{P}^{t\leftarrow M} \rangle + \langle \mathcal{W}^{t\leftarrow p} \rangle = \langle \epsilon \rangle, \tag{3.2}$$

where $\mathcal{P}^{t\leftarrow M}$ is the turbulent energy production rate

$$\mathcal{P}^{t\leftarrow M}(y) = -\overline{u'v'}\frac{\mathrm{d}U}{\mathrm{d}y} \tag{3.3}$$

due to the mean flow and ϵ is the energy dissipation rate of turbulence. In (3.2), $\mathcal{W}^{t\leftarrow p}$ $(= \mathcal{W}^{f\leftarrow p} - \mathcal{W}^{M\leftarrow p})$ is the rate of work done by particles on turbulence. Here, $\mathcal{W}^{f\leftarrow p}$ is the total rate of work by the force $\boldsymbol{f}^{f\leftarrow p}$ that particles exert on the fluid: namely $\mathcal{W}^{f\leftarrow p} = \overline{\boldsymbol{f}^{f\leftarrow p} \cdot \boldsymbol{u}}$. By decomposing the velocity $\boldsymbol{u}$ on the particle surfaces into mean velocity $\boldsymbol{U}$ in the fluid phase and its fluctuation $\boldsymbol{u}'$, the total work can be separated into two contributions:

$$\begin{aligned}\mathcal{W}^{f\leftarrow p} &= \overline{\boldsymbol{f}^{f\leftarrow p}} \cdot \boldsymbol{U} + \overline{\boldsymbol{f}^{f\leftarrow p'} \cdot \boldsymbol{u}'} \\ &= \mathcal{W}^{M\leftarrow p} + \mathcal{W}^{t\leftarrow p}.\end{aligned} \tag{3.4}$$

In a statistically steady state, since the average kinetic energy of particles remains constant, the average rate of work between fluid and particles vanishes, i.e. $\langle \mathcal{W}^{f\leftarrow p} \rangle = 0$. Therefore, when $\langle \mathcal{W}^{t\leftarrow p} \rangle$ is positive, $\langle \mathcal{W}^{M\leftarrow p} \rangle$ must be negative, meaning that particles transfer the kinetic energy from the mean flow to turbulence. Thus, the energy balance equation (3.2) describes the spatially averaged energy budget in turbulence with mean flow. In the following analyses, we investigate how the energy budget is modulated due to particles on the basis of (3.2). Incidentally, we need to take special care to evaluate the energy dissipation rate ϵ in (3.2) accurately in the DNS with IBM (see Appendix B).

3.3. *Turbulent energy production by the mean flow*

We first evaluate the turbulent energy production rate (3.3) due to the mean flow. We show in figure 6 the wall-normal profiles of $\mathcal{P}^{t\leftarrow M}$ in turbulence at $Re_\tau = 512$. Here, we normalise $\mathcal{P}^{t\leftarrow M}(y)$ by the mean turbulent energy dissipation rate $\epsilon_\times(y)$ of the single-phase turbulence. Particle parameters in figure 6 are the same as figure 4; namely

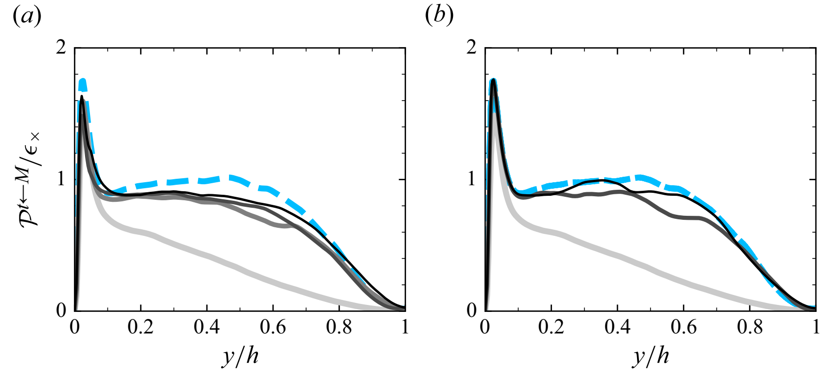

Figure 6. (*a*,*b*) Wall-normal profiles of the mean turbulent energy production rate $\mathcal{P}^{t\leftarrow M}(y)$ (3.3) due to the mean flow at $Re_\tau = 512$. The values are normalised by the mean turbulent energy dissipation rate $\epsilon_\times$ at each height in the single-phase flow. The lines in both panels indicate the same parameters as shown in figure 4.

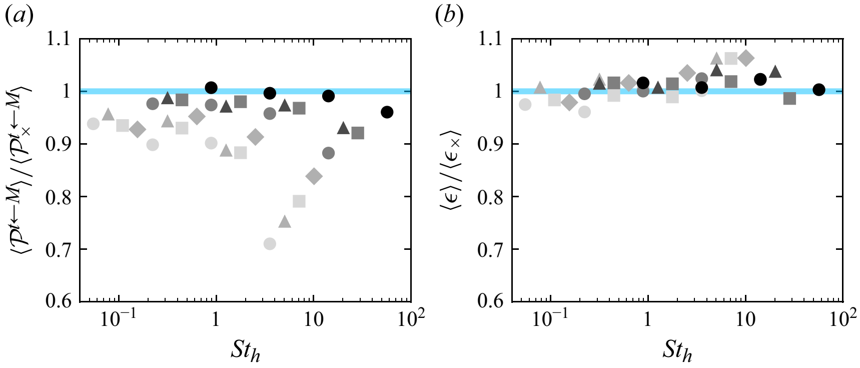

Figure 7. Spatial average of (*a*) turbulent energy production rate $\langle\mathcal{P}^{t\leftarrow M}\rangle$ by the mean flow and (*b*) turbulent energy dissipation rate $\langle\epsilon\rangle$ as functions of St_h. The values are normalised by those in the single-phase flow. The symbols are the same as in figure 5.

figure 6(*a*) shows results for the common D/h $(=0.031)$ but different values of St_h, while figure 6(*b*) shows those for the common St_h $(=3.6)$ but different values of D/h. Figure 6 shows that (i) when the Stokes number is larger or (ii) the particle size is smaller under the condition that the volume fraction is constant, the energy production rate tends to be more reduced. It is also worth noting that the Reynolds stress $(-\overline{u'v'})$ is also reduced (see Appendix C). Since the Reynolds stress is produced by wall-attached vortices (Lozano-Durán *et al.* 2012; Motoori & Goto 2021), turbulent kinetic energy, which is related to these energetic vortices, is also attenuated.

Next, we show in figure 7(*a*) the spatial average $\langle\mathcal{P}^{t\leftarrow M}\rangle$ of the energy production rate normalised by the value $\langle\mathcal{P}_\times^{t\leftarrow M}\rangle$ in the single-phase flow as a function of St_h. The symbols are the same as in figure 5; namely those in lighter colours indicate smaller D/h, and different shapes represent different values of Re_τ. We see that the average production rate gets smaller for (i) larger St_h and (ii) smaller D/h. These behaviours are similar to those for turbulent kinetic energy shown in figure 5.

It is also important to observe that the turbulent energy dissipation rate $\langle\epsilon\rangle$ is not modulated by particles as much as $\langle\mathcal{P}^{t\leftarrow M}\rangle$. Figure 7(*b*) shows $\langle\epsilon\rangle$ normalised by $\langle\epsilon_\times\rangle$ as a function of St_h. Note that ϵ includes the two contributions from the energy dissipation through the energy cascade and from the wake behind added particles. We see that

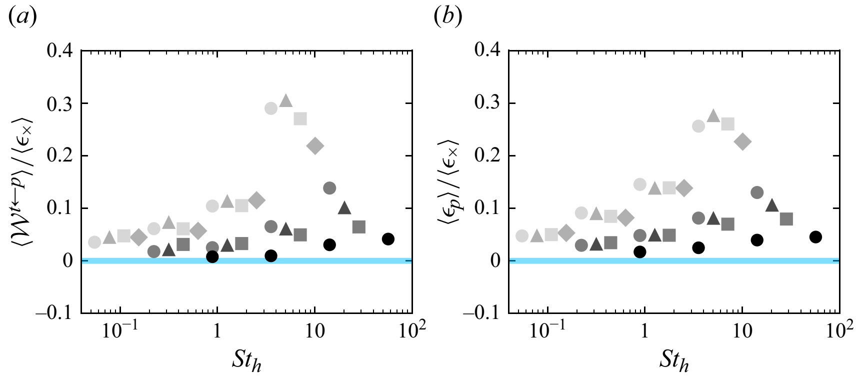

Figure 8. Spatial average of (*a*) rate of work $\mathcal{W}^{t\leftarrow p}$ done by particles on turbulence evaluated by (3.2) and (*b*) energy dissipation rate ϵ_p around particles defined with (3.7) as functions of St_h. The values are normalised by the spatial average $\langle\epsilon_\times\rangle$ of turbulent energy dissipation rate in the single-phase flow. The symbols are the same as in figure 5.

$\langle\epsilon\rangle/\langle\epsilon_\times\rangle$ is close to unity. This result means that the average energy input rate $\langle I^M\rangle$ minus the average energy dissipation rate $\langle\epsilon^M\rangle$ of the mean flow is not significantly altered from that of the single-phase flow. More concretely, $\langle\mathcal{I}^M\rangle$ and $\langle\epsilon^M\rangle$ show similar monotonic trends with respect to St_h (see Appendix D).

3.4. *Additional energy dissipation due to particles*

We have demonstrated in figures 6 and 7(*a*) that particles can reduce the energy production rate $\mathcal{P}^{t\leftarrow M}$, which relates to the attenuation of turbulent kinetic energy. We have also shown in figures 2 and 3 that particle-induced vortices seem relevant to turbulence attenuation. In this subsection, we discuss how these vortices contribute to the reduction of $\mathcal{P}^{t\leftarrow M}$.

For the spatial average in the single-phase flow, the energy production rate due to the mean flow is balanced by the energy dissipation rate, i.e. $\langle\mathcal{P}^{t\leftarrow M}\rangle = \langle\epsilon\rangle$. However, particles can break this balance due to the rate of work $\mathcal{W}^{t\leftarrow p}$ done by particles on turbulence, as described in (3.2). Figure 8(*a*) shows the average of $\mathcal{W}^{t\leftarrow p}$ evaluated by (3.2). We see that $\langle\mathcal{W}^{t\leftarrow p}\rangle$ gets larger for particles with larger St_h and smaller D/h. This implies that particles play a role in transferring turbulent kinetic energy from the mean flow to turbulence. As a result, vortex rings shown in figures 2 and 3 are generated. Then, the turbulent kinetic energy associated with these vortices is rapidly dissipated, leading to a substantial energy dissipation rate ϵ_p around the particles. Therefore, combining the local balance $\mathcal{W}^{t\leftarrow p} = \epsilon_p$ with (3.2), we can describe the energy production rate as

$$\langle\mathcal{P}^{t\leftarrow M}\rangle = \langle\epsilon\rangle - \langle\epsilon_p\rangle. \tag{3.5}$$

Since $\langle\epsilon\rangle = \langle\epsilon_\times\rangle$ approximately holds in the present system as shown in figure 7(*b*), we can rewrite (3.5) as

$$1 - \frac{\langle\mathcal{P}^{t\leftarrow M}\rangle}{\langle\mathcal{P}^{t\leftarrow M}_\times\rangle} = \frac{\langle\epsilon_p\rangle}{\langle\epsilon_\times\rangle}. \tag{3.6}$$

This equation means that the degree of the reduction of $\langle\mathcal{P}^{t\leftarrow M}\rangle$ is proportional to the energy dissipation rate $\langle\epsilon_p\rangle$ due to vortices induced by particles.

To verify the above argument, we show in figure 8(*b*) the spatial average $\langle\epsilon_p\rangle$ of the energy dissipation rate ϵ_p around particles normalised by $\langle\epsilon_\times\rangle$. Here, to estimate $\langle\epsilon_p\rangle$, we numerically compute the local average of the turbulent energy dissipation rate around all particles:

$$\langle \epsilon_p \rangle = \frac{1}{V_{box}} \left(\left\langle \int_{\Omega_{\circledcirc}} \epsilon(\boldsymbol{x}', t)\, \mathrm{d}V' \right\rangle - V_{\circledcirc} \langle \epsilon \rangle \right). \tag{3.7}$$

Here, $\Omega_{\circledcirc}$ denotes the region between a spherical particle and another sphere with diameter $3D$ concentric with the particle (Sun *et al.* 2024), $V_{\circledcirc}$ is the volume of $\Omega_{\circledcirc}$ and V_{box} is the volume of the computational box. The first term on the right-hand side of (3.7) captures the local average of the energy dissipation rate ϵ around particles, where we evaluate ϵ by (B2) in Appendix B. Since this quantity includes the dissipation rates due to not only the vortices created around particles but also vortices generated by energy cascade or the mean shear, we subtract the latter contribution expressed by the second term. Figure 8(*b*) shows that $\langle \epsilon_p \rangle$ gets larger for larger St_h or smaller D/h, which is similar to the behaviour of $\langle \mathcal{W}^{t \leftarrow p} \rangle$ in figure 8(*a*). We can explain these dependences by noting that the local energy dissipation rate per unit mass around a single particle is approximated by $|\Delta u|^3/D$, where Δu is the magnitude of the relative velocity. Hence, when (i) the Stokes number is larger, and therefore the relative velocity is larger or (ii) the diameter is smaller, ϵ_p gets larger under the condition that the particle volume fraction is fixed. Recall that figure 7(*a*) shows a similar tendency for the average reduction rate $\langle \mathcal{P}^{t \leftarrow M} \rangle$. To verify this similarity, we show $1 - \langle \mathcal{P}^{t \leftarrow M} \rangle / \langle \mathcal{P}^{t \leftarrow M}_{\times} \rangle$ as a function of $\langle \epsilon_p \rangle / \langle \epsilon_{\times} \rangle$ in figure 9(*a*). The data approximately collapse on the red dotted line. This implies that we can describe the average reduction rate of the energy production $\langle \mathcal{P}^{t \leftarrow M} \rangle$ due to the mean flow in terms of the additional energy dissipation rate $\langle \epsilon_p \rangle$ by particles, as indicated by (3.6). Incidentally, although some plots lie beneath the red line, this deviation arises from the slight modulation of $\langle \epsilon \rangle$ from the single-phase flow (see figure 7*b*). Taking this effect into account, when we replot the attenuation rate of $\langle \mathcal{P}^{t \leftarrow M} \rangle$ as a function of the energy flux $\langle \epsilon \rangle - \langle \epsilon_p \rangle$ in figure 9(*b*), the plots collapse better.

Moreover, the additional energy dissipation rate is also important in describing the average attenuation rate of turbulent kinetic energy. We show in figure 9(*c*) the average attenuation rate $\mathcal{A}$, defined as (3.1), of turbulent kinetic energy. Although the turbulence attenuation rate depends on St_h, D/h and Re_τ (see figure 5), when plotting $\mathcal{A}$ as a function of $\langle \epsilon_p \rangle / \langle \epsilon_{\times} \rangle$, the data approximately collapse on the red dotted line. We conclude therefore that the turbulence attenuation rate is related to the additional energy dissipation rate $\langle \epsilon_p \rangle$ due to particles. This is consistent with previous studies on modulation of wall-bounded turbulence by pointwise particles (Zhao *et al.* 2013) and fixed particles with restricted motion (Peng *et al.* 2019*b*), which emphasised the importance of the additional energy dissipation around particles. Incidentally, in figure 9(*c*), we observe the proportionality between $\mathcal{A}$ and $\langle \epsilon_p \rangle / \langle \epsilon_{\times} \rangle$, indicating that $\langle \mathcal{P}^{t \leftarrow M} \rangle$ is proportional to $\langle K \rangle$. However, there may be a better expression for the relationship between $\mathcal{P}^{t \leftarrow M}$ and K for higher-Reynolds-number turbulence. We further discuss this in § 4.3.

We summarise the mechanism of attenuation of wall-bounded turbulence. When particles cannot follow the fluid motions and create small vortices around them (figures 2 and 3), turbulent kinetic energy K is attenuated (figure 4). This occurs because these particle-induced vortices acquire a part of the kinetic energy from the mean flow (figure 8*a*), and produce the additional energy dissipation rate (figure 8*b*), thereby preventing energy transfer rate $\mathcal{P}^{t \leftarrow M}$ from the mean flow to turbulent vortices (figures 6 and 7*a*). This is the reason why we can describe the average attenuation rates of $\mathcal{P}^{t \leftarrow M}$ and K in terms of the additional energy dissipation rate $\langle \epsilon_p \rangle$ due to particles (figure 9).

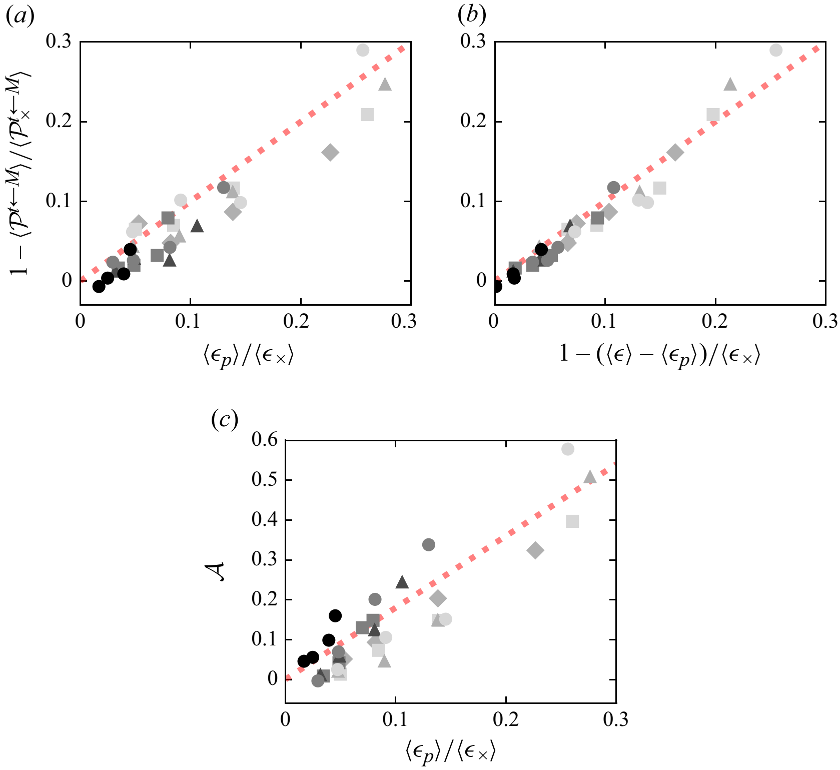

Figure 9. Average attenuation rate of turbulent energy production rate $\langle \mathcal{P}^{t\leftarrow M} \rangle$ by the mean flow as functions of (*a*) $\langle \epsilon_p \rangle / \langle \epsilon_{\times} \rangle$ and (*b*) $1 - (\langle \epsilon \rangle - \langle \epsilon_p \rangle)/\langle \epsilon_{\times} \rangle$. (*c*) Average attenuation rate $\mathcal{A}$ of turbulent kinetic energy as a function of $\langle \epsilon_p \rangle / \langle \epsilon_{\times} \rangle$. The symbols are the same as in figure 5. The proportional coefficients of the red dotted lines are (*a*,*b*) 1 and (*c*) 1.8.

Incidentally, it is also worth mentioning that the Reynolds stress is also reduced (figure 15*b* in Appendix C), leading to a reduction of the frictional drag coefficient. This is because the mean bulk velocity increases (figure 15*a*) as a consequence of the reduction of fluid momentum transfer in the wall-normal direction. We show this result in Appendix E.

4. Prediction of turbulence attenuation rate

In this section, we propose a method to predict the degree of turbulence attenuation in terms of the given property of particles. To this end, we must predict the additional energy dissipation rate $\langle \epsilon_p \rangle$, which determines the turbulence attenuation rate, without the direct evaluation (3.7) as in the previous section.

4.1. *Estimation of particle energy dissipation*

We first consider the magnitude of the force exerted on a particle by the fluid:

$$F^{p\leftarrow f} = \frac{1}{2} C_D \rho_f |\Delta u|^2 A, \tag{4.1}$$

where C_D is the drag coefficient, A $(=\pi D^2/4)$ is the cross-sectional area of the sphere and Δu is the magnitude of the relative velocity. The particle subjected to this force leads

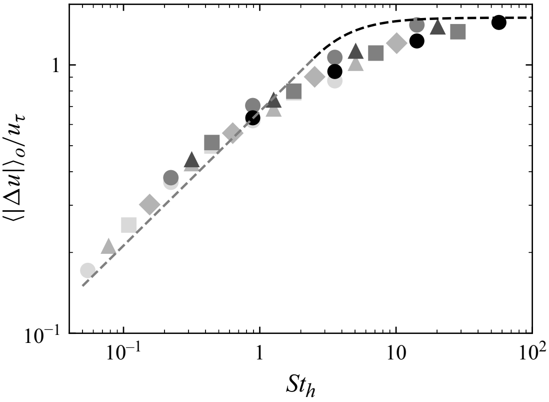

Figure 10. Relative velocity $\langle |\Delta u| \rangle_o$ between particles and their surrounding fluid averaged in the outer layer. The symbols are the same as in figure 5. The grey and black dashed lines are evaluation by (4.5*a*) and (4.5*b*), respectively, with coefficients of $u_L = 1.5 u_\tau$ and $\tau_L = 2.5 \tau_h$.

to energy dissipation at the rate of $F^{p \leftarrow f} \Delta u$. Therefore, the energy dissipation rate due to all the particles in the system can be expressed as

$$\langle \epsilon_p^{\#} \rangle = \frac{3}{4} \varLambda_0 C_D \frac{|\Delta u|^3}{D}. \tag{4.2}$$

Thus, to obtain $\langle \epsilon_p^{\#} \rangle$, we need to estimate the relative velocity Δu. We discuss the estimation of Δu in the next subsection.

Moreover, by estimating the average energy dissipation rate in the single-phase flow as $\langle \epsilon_\times^{\#} \rangle = u_L^3 / h$ with u_L $(\sim u_\tau)$ being the characteristic velocity at the largest scale in the outer layer, we obtain

$$\frac{\langle \epsilon_p^{\#} \rangle}{\langle \epsilon_\times^{\#} \rangle} = \frac{3}{4} \varLambda_0 C_D \frac{h}{D} \frac{|\Delta u|^3}{u_L^3}. \tag{4.3}$$

For the drag coefficient C_D, we use the experimental law (Schiller 1933):

$$C_D = \frac{24}{Re_D} \left(1 + 0.15 Re_D^{0.687} \right), \tag{4.4}$$

where Re_D $(= |\Delta u| D / \nu)$ is the particle Reynolds number. Thus, we can describe the additional energy dissipation rate (4.3) by using the particle parameters ($\varLambda_0$ and D/h) and the relative velocity Δu.

4.2. *Relative velocity*

We show in figure 10 the relative velocity $\langle |\Delta u| \rangle_o$ averaged in the outer layer $(y/h \geqslant 0.3)$ as a function of St_h. Note that since Δu strongly depends on height y, we focus on the outer layer where Δu weakly depends on y (see Appendix F). Here, we evaluate the relative velocity as $\Delta u = \langle u \rangle_{ⓟ} - u_p$, where we define the surrounding fluid velocity $\langle u \rangle_{ⓟ}$ for each particle by the average fluid velocity on the surface of a sphere with diameter $2D$ concentric with the particle (Kidanemariam *et al.* 2013; Uhlmann & Chouippe 2017). Symbols in lighter colours indicate smaller D/h, and different shapes represent different values of Re_τ. We see in the figure that St_h determines the relative velocity irrespective of the other parameters. We also see that the functional forms of the relative velocity are well approximated by the dashed lines, which are defined as

$$|\Delta u| = \begin{cases} \dfrac{(\tau_p/\tau_L)^{1/2}}{\sqrt{2}}\, u_L & (\tau_\eta \leqslant \tau_p \leqslant \tau_L), \qquad (4.5a) \\ \dfrac{\tau_p/\tau_L}{\sqrt{1+(\tau_p/\tau_L)^2}}\, u_L & (\tau_p > \tau_L). \qquad (4.5b) \end{cases}$$

Here, (4.5a) holds when the particle relaxation time τ_p is longer than the Kolmogorov time τ_η and shorter than the integral time τ_L, whereas (4.5b) holds for $\tau_p > \tau_L$. We can derive (4.5) by assuming pointwise heavy particles based on the argument by Balachandar (2009) as follows. As considered in our previous studies (Oka & Goto 2021; Motoori, Wong & Goto 2022), we first assume that the motion of particles with τ_p is independent of fluid motions smaller than ℓ, where ℓ is the length scale such that the turnover time $\tau^{(\ell)}$ $(= \langle \epsilon_\times \rangle^{-1/3} \ell^{2/3})$ of vortices with size ℓ is approximately τ_p, i.e. $\ell = \langle \epsilon_\times \rangle^{1/2} \tau_p^{3/2}$. Then, considering a particle in the oscillating flow with frequency $\tau^{(\ell)}$ (Balachandar 2009), we obtain

$$|\Delta u| = \frac{\tau_p/\tau^{(\ell)}}{\sqrt{1+(\tau_p/\tau^{(\ell)})^2}}\, \widetilde{u}^{(\ell)}. \qquad (4.6)$$

Here, $\widetilde{u}^{(\ell)}$ is the fluid velocity coarse-grained at scale ℓ. For $\tau_\eta \leqslant \tau_p \leqslant \tau_L$, when assuming that the relative velocity is determined by vortices whose turnover time is comparable to the particle relaxation time (i.e. $\tau^{(\ell)} = \tau_p$), we can obtain (4.5a). In this derivation, we use $\widetilde{u}^{(\ell)} = (\tau^{(\ell)}/\tau_L)^{1/2} u_L$. On the other hand, we can obtain (4.5b) for $\tau_p > \tau_L$ by assuming that the relative velocity is determined by the largest-scale vortices (i.e. $\tau^{(\ell)} = \tau_L$).

Figure 10 shows that (4.5) is in good agreement with our DNS data. Here, we choose the parameters u_L and τ_L in (4.5) as in the order of u_τ and τ_h, respectively, so that the curves expressed by (4.5) fit our data. Incidentally, the relative velocity for $\tau_p < \tau_\eta$ is determined by vortices at the Kolmogorov time scale (i.e. $\tau^{(\ell)} = \tau_\eta$), although in the present study, we do not simulate particles with $\tau_p < \tau_\eta$.

Incidentally, it is not always possible to estimate the relative velocity using (4.5). This evaluation is valid when the particle diameter is smaller than the length scale ℓ of vortices with the turnover time $\tau^{(\ell)} \approx \tau_p$, i.e.

$$D \lesssim \ell \quad \Leftrightarrow \quad \frac{D}{h} \lesssim \begin{cases} (\tau_p/\tau_L)^{3/2} \approx St_h^{3/2} & (\tau_\eta \leqslant \tau_p \leqslant \tau_L), \qquad (4.7a) \\ 1 & (\tau_p > \tau_L). \qquad (4.7b) \end{cases}$$

The examined particles satisfy this condition.

4.3. *Prediction of turbulence attenuation rate*

By substituting the relative velocity prediction (4.5) into (4.3), we can estimate the additional energy dissipation rate by

$$\frac{\langle \epsilon_p^\# \rangle}{\langle \epsilon_\times^\# \rangle} = \begin{cases} \dfrac{3}{4} \Lambda_0 C_D \dfrac{h}{D} \dfrac{(\tau_p/\tau_L)^{3/2}}{2\sqrt{2}} & (\tau_\eta \leqslant \tau_p \leqslant \tau_L), \qquad (4.8a) \\ \dfrac{3}{4} \Lambda_0 C_D \dfrac{h}{D} \dfrac{(\tau_p/\tau_L)^3}{(1+(\tau_p/\tau_L)^2)^{3/2}} & (\tau_p > \tau_L). \qquad (4.8b) \end{cases}$$

We plot in figure 11 the average attenuation rate $\mathcal{A}$ as a function of $\langle \epsilon_p^\# \rangle / \langle \epsilon_\times^\# \rangle$. We see that our DNS data collapse onto a single line, which is approximated by the red dotted line. In this figure, we also plot the experimental results (Kulick *et al.* 1994) for turbulent channel

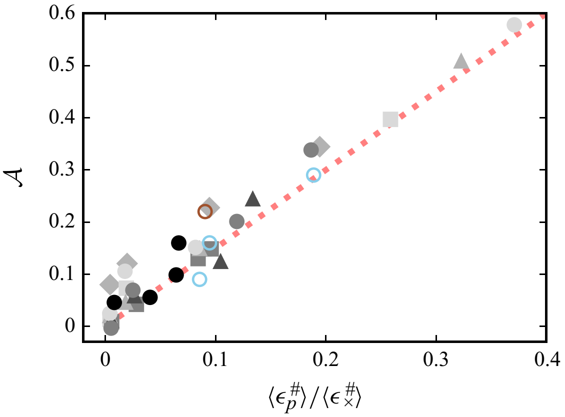

Figure 11. Average attenuation rate $\mathcal{A}$ of turbulent kinetic energy as a function of $\langle \epsilon_p^\# \rangle / \langle \epsilon_\times^\# \rangle$, which is estimated by (4.8) using only particle parameters. Particle parameters for the filled symbols are the same as in figure 5. The open circles show the turbulence attenuation rate at the channel centre measured in experiments by Kulick *et al.* (1994). The brown and light blue symbols indicate the results for copper and glass particles (with different volume fractions Λ_0), respectively. The proportional coefficient of the red dotted line is 1.5.

flow. The brown and light blue open symbols indicate the attenuation rates at the channel centre by copper and glass particles, respectively. Despite the different particle types and volume fractions, the experimental data align closely with our DNS results. Thus, we can use (4.8) to estimate the additional energy dissipation rate $\langle \epsilon_p^\# \rangle / \langle \epsilon_\times^\# \rangle$, and by using this estimation, we can describe the turbulence attenuation rate.

Before concluding this article, we discuss the relevance to the study on periodic turbulence by Oka & Goto (2022). They derived the formula

$$1 - \left(1 - \frac{\mathcal{A}}{1+\alpha}\right)^{3/2} = \frac{\langle \epsilon_p \rangle}{\langle \epsilon_\times \rangle} \tag{4.9}$$

for describing the turbulence attenuation rate, and then verified it using their DNS results of periodic turbulence. Here, α is the ratio of the kinetic energy of the mean flow to turbulent energy for the single-phase flow. When deriving this formula, they first assumed that the additional energy dissipation rate bypasses the energy cascade. Then, they used the dissipation law of Taylor (1935) to relate average turbulent kinetic energy $\langle K \rangle$ to its dissipation rate $\langle \epsilon \rangle$. We may use a similar relation between K and ϵ $(= \mathcal{P}^{t \leftarrow M})$ in the log layer for wall turbulence at sufficiently high Reynolds numbers. However, since the present turbulence does not have a large scale separation to discuss the buffer, log and outer layers individually, we have argued the spatially averaged quantities. Nevertheless, our DNS results show that the turbulence attenuation rate increases monotonically with respect to $\langle \epsilon_p \rangle / \langle \epsilon_\times \rangle$ (see figure 9*c*). Moreover, we have demonstrated in figure 11 that $\langle \epsilon_p \rangle / \langle \epsilon_\times \rangle$ can be estimated based solely on particle parameters using (4.8). This estimation can be applicable to developed turbulence laden with small particles satisfying (4.7) in a dilute regime.

5. Conclusions

To investigate the attenuation of wall-bounded turbulence due to heavy small particles in a dilute regime, we have conducted DNS of turbulent channel flow laden with finite-size solid particles. Fixing the small volume fraction (0.82 %) of particles, we change the particle diameter, particle relaxation time and turbulence Reynolds number (table 1). The conclusions of the present study are as follows.

When particles cannot follow the ambient fluid, namely when the particle relaxation time is longer than the swirling time of the wall-attached vortices at the particles' existing height, vortex rings are created by the particles (figures 2 and 3). The presence of such particle-induced vortices results in a significant turbulence attenuation (figures 4 and 5). This is because they produce additional energy dissipation (figure 8*b*), which bypasses the energy production from the mean flow to turbulent vortices (figures 6, 7*a* and 8*a*). This reduction of the energy production (figure 6) is caused by the attenuation of turbulent vortices which are relevant to the production of the Reynolds stress (figure 15*b*); consequently, turbulent kinetic energy is also attenuated. In contrast, the energy dissipation rate is not significantly modulated in the examined cases (figure 7*b*). Therefore, the energy production rate is described solely by the additional energy dissipation rate ϵ_p. Our DNS results (figure 9*a*) show that this energy balance, described by (3.6), holds for the spatial averaging by numerically evaluating the additional energy dissipation rate $\langle \epsilon_p \rangle$ (3.7). We also show that we can describe the average attenuation rate $\mathcal{A}$ (3.1) of turbulent kinetic energy in terms of $\langle \epsilon_p \rangle$ (figure 9*c*). This attenuation mechanism well explains the Stokes-number and particle-diameter dependence of $\langle K \rangle$ (figure 5), since the energy dissipation rate $\langle \epsilon_p \rangle$ due to particles becomes larger as (i) the Stokes number becomes larger or (ii) the particle size becomes smaller under the condition that the volume fraction is constant (figure 8*b*).

To quantitatively predict the degree of turbulence attenuation, we estimate the relative velocity required for the estimation (4.3) of the additional energy dissipation rate $\langle \epsilon_p^{\#} \rangle / \langle \epsilon_\times^{\#} \rangle$. Our DNS results (figure 10) demonstrate that the relative velocity averaged in the outer layer is determined by the functions (4.5) of St_h. These are derived based on the argument by Balachandar (2009) for heavy pointwise particles, allowing us to quantify $\langle \epsilon_p^{\#} \rangle / \langle \epsilon_\times^{\#} \rangle$ only from particle properties through (4.8). Moreover, our estimation of the average turbulence attenuation in terms of $\langle \epsilon_p^{\#} \rangle / \langle \epsilon_\times^{\#} \rangle$ well describes not only the present DNS data but also previous experimental results by Kulick *et al.* (1994) (figure 11).

Acknowledgements. We would like to thank Professor Uhlmann for discussing the present study during our stay in Karlsruhe. We also thank Professor Balachandar for discussing the evaluation of the relative velocity.

Funding. This study was partly supported by JSPS Grants-in-Aid for Scientific Research 20H02068 and 23K13253. The DNS were conducted by using the computational resources of the supercomputers Fugaku through the HPCI System Research Projects (hp220232, hp230288 and hp240278). The numerical analyses were conducted under the auspices of the NIFS Collaboration Research Program (NIFS22KISS010 and NIFS24KISC007).

Declaration of interests. The authors report no conflict of interest.

Appendix A. Indicator proposed by Yu *et al.* (2021) for turbulence enhancement

In the present study, turbulence enhancement does not occur because of the absence of gravity. Yu *et al.* (2021) introduced the indicator defined as

$$\chi = \frac{Re_p}{Re_b^{0.33}\,(D/h)^{0.61}\,(\rho_p/\rho_f)^{0.05}}, \tag{A1}$$

by fitting their DNS results, and demonstrated that turbulence enhancement occurs for $\chi \gtrsim 20$. This condition requires large Re_p, which is also a known condition for turbulence enhancement (Uhlmann 2008; Balachandar & Eaton 2010). However, since the relative velocity in the present system without gravity is of the order of the fluctuation fluid velocity

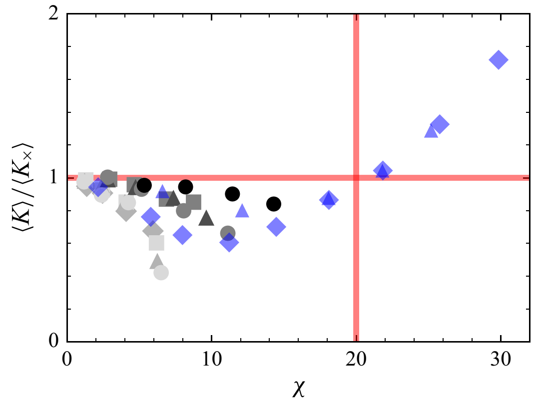

Figure 12. Spatial average $\langle K\rangle$ of turbulent kinetic energy normalised by the value $\langle K_\times\rangle$ in the single-phase flow as a function of the indicator χ defined as (A1). The grey symbols are the same as in figure 5. The blue symbols show the results by Yu *et al.* (2021) for particles with $D/h = 0.1$, $\rho_p/\rho_f = 2$ and $\Lambda_0 = 0.0236$ but with different values of the settling velocity u_g in turbulent channel flow at $Re_\tau \approx 350$ (triangles) and 180 (diamonds).

at most (figure 10), Re_p is much smaller than Re_b. Therefore, the condition $\chi \gtrsim 20$ is not satisfied, as shown with the grey symbols in figure 12. This is consistent with the fact that we observe only attenuation in the present system. In contrast, the blue symbols show the results by Yu *et al.* (2021) for small particles ($D^+ \approx 10$) at $Re_\tau \approx 350$ (triangles) and 180 (diamonds) in the presence of gravity. When χ is larger than 20 due to the gravitational effect, the average turbulent kinetic energy is enhanced.

Appendix B. Evaluation of energy dissipation rate

In this appendix, we describe how to accurately evaluate the energy dissipation rate $\epsilon = 2\nu \mathbf{S} : \mathbf{S}$, where $\mathbf{S}$ is the strain-rate tensor, in DNS using the IBM. In each numerical step of the IBM, we first ignore the presence of particles to obtain the preliminary velocity $\boldsymbol{u}^*$ by integrating the Navier–Stokes equation. We then evaluate the body force to eliminate the velocity difference between $\boldsymbol{u}^*$ and the velocity $\boldsymbol{u}_s$ on the particle surface. For particles, the force $\boldsymbol{F}_\ell^{IBM}$ acts on the Lagrangian points (the ℓth point is denoted by $\boldsymbol{x}_\ell$) distributed on the particle surface; whereas the fluid is forced by $\boldsymbol{f}_\ell^{IBM} = -\boldsymbol{F}_\ell^{IBM}\delta(\boldsymbol{x} - \boldsymbol{x}_\ell)$ on grid points $\boldsymbol{x}$ around $\boldsymbol{x}_\ell$, where δ is a regularised delta function satisfying $\int_{\Omega_\ell} \delta(\boldsymbol{x} - \boldsymbol{x}_\ell)\,\mathrm{d}V = 1$ with Ω_ℓ being the spherical region with centre at $\boldsymbol{x}_\ell$ and radius 1.5Δ. Note that the sum of the rates of work due to $\boldsymbol{F}_\ell^{IBM}$ and $\boldsymbol{f}_\ell^{IBM}$ is expressed by

$$W_\ell^{IBM} + w_\ell^{IBM} = -\int_{\Omega_\ell} \boldsymbol{f}_\ell^{IBM} \cdot (\boldsymbol{u}_s(\boldsymbol{x}_\ell) - \boldsymbol{u}(\boldsymbol{x}))\,\mathrm{d}V. \tag{B1}$$

Here, W_ℓ^{IBM} $(= \boldsymbol{F}_\ell^{IBM} \cdot \boldsymbol{u}_s)$ is the rate of work due to $\boldsymbol{F}_\ell^{IBM}$, whereas w_ℓ^{IBM} $(= \int_{\Omega_\ell} \boldsymbol{f}_\ell^{IBM} \cdot \boldsymbol{u}\,\mathrm{d}V)$ is the rate of work due to $\boldsymbol{f}_\ell^{IBM}$. The total rate of work (B1) does not vanish because of the velocity difference $\boldsymbol{u}_s - \boldsymbol{u}$, which results in extra energy dissipation, as numerically demonstrated below. Therefore, in the present analyses, we take into account this contribution due to the IBM, and we evaluate turbulent energy dissipation rate as

$$\epsilon = 2\nu \mathbf{S} : \mathbf{S} + \sum_\ell \boldsymbol{f}_\ell^{IBM} \cdot (\boldsymbol{u}_s(\boldsymbol{x}_\ell) - \boldsymbol{u}(\boldsymbol{x})). \tag{B2}$$

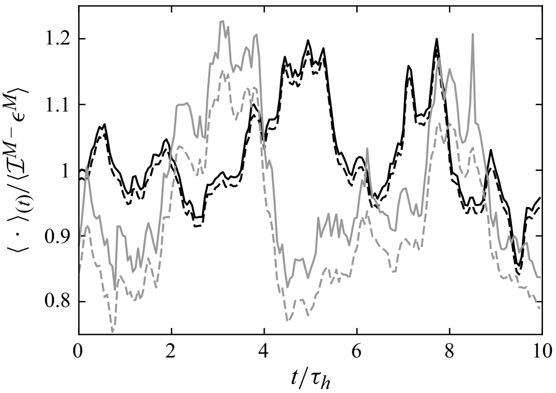

Figure 13. Spatial average $\langle\,\cdot\,\rangle_{(t)}$ at time t for turbulent energy dissipation rate ϵ (solid line) estimated by (B2) and that for ϵ^* (dashed line) in the case ignoring the second term of (B2). The black and grey lines show the results for $St_h = 0.16$ and 10, respectively, for turbulence at $Re_\tau = 180$. The values are normalised by $\langle\mathcal{I}^M - \epsilon^M\rangle$, which is balanced with the time average $\langle\epsilon\rangle$ of $\langle\epsilon\rangle_{(t)}$.

Here, we use the value of $\mathbf{S}$ evaluated in the DNS, and $\sum_\ell$ denotes the summation over the Lagrangian points $\boldsymbol{x}_\ell$ located within the distance $1.5\varDelta$ from $\boldsymbol{x}$.

To verify the above argument, we show the spatial average $\langle\,\cdot\,\rangle_{(t)}$ of ϵ at each time t by the solid line in figure 13. The dashed line is the average $\langle\epsilon^*\rangle_{(t)}$ $(=\langle 2\nu\mathbf{S}:\mathbf{S}\rangle_{(t)})$ in the case ignoring the second term of (B2). The black and grey lines show the results for $St_h = 0.16$ and 10, respectively. We see that the discrepancy between the solid and dashed lines is non-negligible especially for larger St_h. Note that the solid line always lies above the dashed one, which means that the second term of (B2) contributes to energy dissipation. We explain this by rewriting the summand as

$$\boldsymbol{f}_\ell^{IBM}\cdot(\boldsymbol{u}_s - \boldsymbol{u}) \approx \frac{(\boldsymbol{u}_s - \boldsymbol{u})^2}{\Delta t}\,\delta(\boldsymbol{x} - \boldsymbol{x}_\ell) > 0 \tag{B3}$$

because $\boldsymbol{F}_\ell^{IBM} = -(\boldsymbol{u}_s - \boldsymbol{u}^*)/\Delta t$ and $\boldsymbol{u}^*$ is close to $\boldsymbol{u}$. We also verify (B2) by the energy budget that the temporal average $\langle\epsilon\rangle$ of $\langle\epsilon\rangle_{(t)}$ is balanced with the average energy input rate $\langle\mathcal{I}^M\rangle$ minus the average energy dissipation rate $\langle\epsilon^M\rangle$ in the mean flow. We have confirmed that the balance is satisfied with an error within 1 %, and if we ignored the second term in (B2), the average value $\langle\epsilon^*\rangle$ would give a discrepancy of 8 % to $\langle\mathcal{I}^M - \epsilon^M\rangle$ for $St_h = 10$. We therefore evaluate ϵ using (B2) in the present study.

Thus, the contribution of the second term of (B2) to energy dissipation rate is non-negligible. However, this does not mean that the present DNS is not enough to resolve energy dissipation rate field around particles, although the second term vanishes in the limit of infinite resolution. Figure 14 shows the average distribution of energy dissipation rate ϵ on the two-dimensional plane (x', z') that passes through the particle centre. The results are for particles with $D/h = 0.089$ and $St_h = 10$ existing at the channel centre in turbulence at $Re_\tau = 180$. Figure 14(*a*) shows the case with the resolution $(D/\varDelta = 8)$ in the present DNS; while figure 14(*b*) shows the case with twice the resolution $(D/\varDelta = 16)$. We see that the higher resolution captures stronger ϵ near the particle interface, as was also observed by Xia *et al.* (2022). It is, however, important to note that since the energy dissipation rate is more widely distributed for the lower resolution, average values are almost the same; more specifically, 0.20 and 0.21 in wall units. Therefore, the present resolution is sufficient to estimate the average energy dissipation rate ϵ_p around particles, which is a key quantity for average attenuation rate of turbulence.

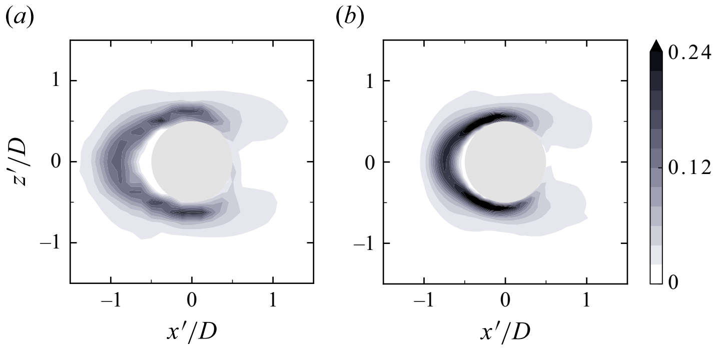

Figure 14. Average spatial distribution of turbulent energy dissipation rate ϵ around a particle with $D/h = 0.089$ and $St_h = 10$ located at the channel centre in turbulence at $Re_\tau = 180$. The results are obtained using the different DNS resolutions (*a*) $D/\Delta = 8$ and (*b*) 16. The values are shown in wall units.

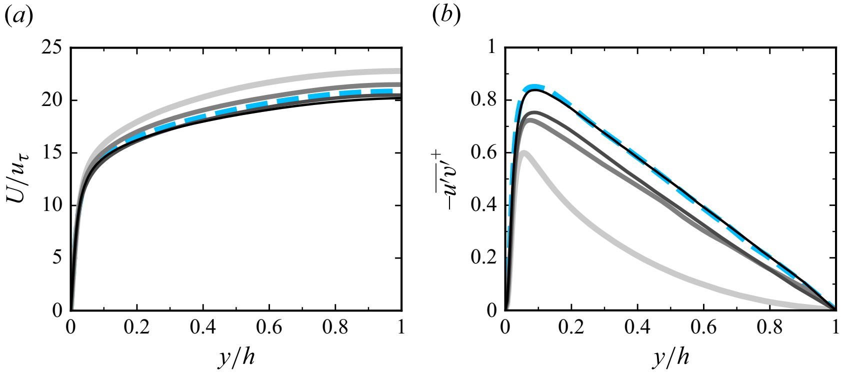

Figure 15. Wall-normal profiles of (*a*) the mean streamwise velocity $U(y)$ and (*b*) Reynolds stress $-\overline{u'v'}(y)$ at $Re_\tau = 512$. The lines indicate the same parameters as shown in figures 4(*a*) and 6(*a*).

Appendix C. Mean velocity and Reynolds stress

We have shown in figure 6 the significant reduction of energy production rate $\mathcal{P}^{t\leftarrow M}$ from the mean flow. In this appendix, to show that this reduction is due to the attenuation of the Reynolds stress, we show in figure 15 the wall-normal profiles of the mean streamwise velocity U and Reynolds stress $-\overline{u'v'}$ at $Re_\tau = 512$. Particle parameters are the same as in figure 6(*a*); namely the results for the common D/h $(= 0.031)$ but different values of St_h. Looking at figure 15(*a*), we notice that the mean velocity is not markedly modulated from the single-phase flow (blue dashed line). More precisely, the mean bulk velocity slightly increases with St_h, which is related to the reduction of the Reynolds stress. This is verified by figure 15(*b*), where we see that the Reynolds stress is attenuated more significantly as St_h gets larger.

Appendix D. Energy input rate and dissipation rate in the mean flow

Figure 16 shows the averages of energy input rate $\mathcal{I}^M$ $(= Uf_x^{ex})$ due to the external pressure gradient and energy dissipation rate ϵ^M $(= \nu(\mathrm{d}U/\mathrm{d}y)^2)$ in the mean flow. These quantities show similar monotonic trends for St_h due to the slight modulation of the

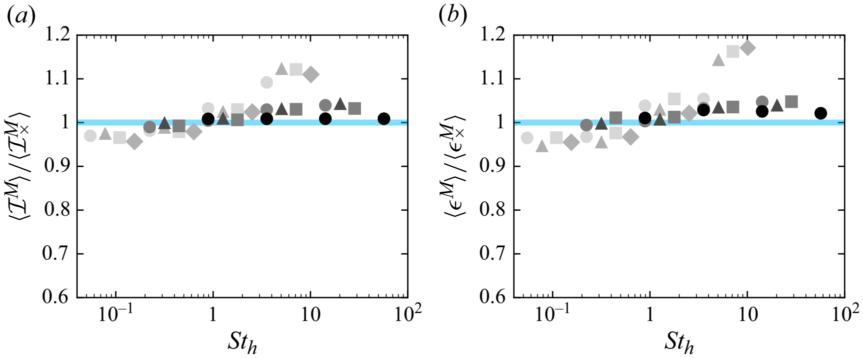

Figure 16. Spatial average of (*a*) energy input rate $\mathcal{I}^M$ due to the external pressure gradient and (*b*) energy dissipation rate ϵ^M in the mean flow. The values are normalised by those in the single-phase flow. The symbols are the same as in figure 5.

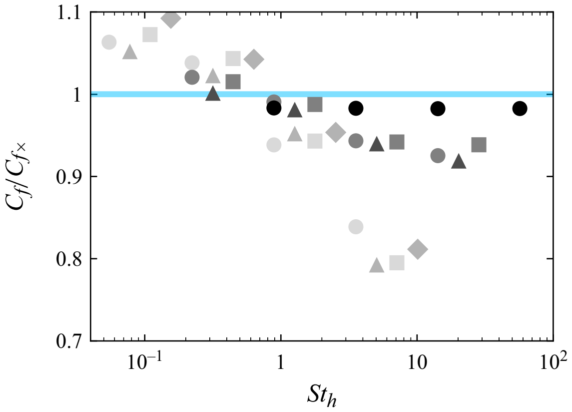

Figure 17. Frictional drag coefficient C_f normalised by the value in the single-phase flow. The symbols are the same as in figure 5.

mean velocity (figure 15*a*). As a result, the difference between these quantities, that is, the turbulent dissipation rate $\langle \epsilon \rangle$ $(= \langle \mathcal{I}^M \rangle - \langle \epsilon^M \rangle)$, is only slightly modulated (figure 7*b*).

Appendix E. Drag reduction

We show in figure 17 the friction drag coefficient C_f normalised by the value in the single-phase flow as a function of St_h, where $C_f = \tau_w/(\rho_f U_b^2/2) = 2u_\tau^2/U_b^2$ with τ_w being the average frictional stress on the walls. Note that in the present study, the external pressure gradient to drive the flow and therefore the frictional stress τ_w are constant; while the mean bulk velocity U_b can be modulated due to the presence of particles. Therefore, larger (or smaller) U_b means smaller (or larger) C_f. We see in figure 17 that for $St_h \gtrsim 1$, the ratio $C_f/C_{f\times}$ is less than 1. More concretely, C_f gets smaller for larger St_h and smaller D/h. This is similar to the behaviour of average turbulent kinetic energy (figure 5) and Reynolds stress (figure 15*b*). We therefore conclude that when turbulence is attenuated, the frictional drag coefficient is also reduced. Drag modulations were also investigated in turbulent channel flow laden with spheroidal particles (Ardekani *et al.* 2017; Ardekani

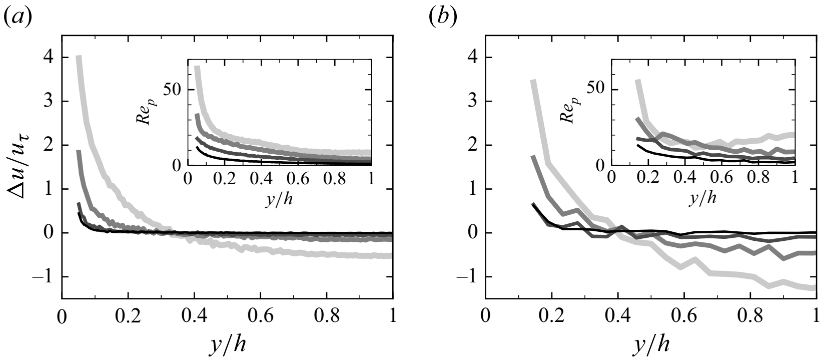

Figure 18. Wall-normal profiles of the mean relative velocity $\Delta u(y)$ for $D^+ = 16$ (i.e. (*a*) $D/h = 0.031$ and (*b*) 0.089) in turbulence at (*a*) $Re_\tau = 512$ and (*b*) 180. The four lines in each panel show, from the thinner (and darker) to thicker (and lighter), (*a*) $St_h = 0.056$, 0.22, 0.89 and 3.6, and (*b*) $St_h = 0.16$, 0.63, 2.5 and 10. The insets show the particle Reynolds number $Re_p(y)$.

& Brandt 2019), neutrally buoyant spheres (Picano, Breugem & Brandt 2015) and small heavy ones (Yu *et al.* 2017; Costa *et al.* 2021; Dave & Kasbaoui 2023).

Appendix F. Wall-normal profile of the relative velocity

As mentioned in § 4.2, the relative velocity depends strongly on height. We can confirm this in figure 18, which shows the wall-normal profiles of the mean streamwise velocity difference $\Delta u(y)$ for $Re_\tau = 512$ and 180. These results are for common D/h at each Re_τ but for different St_h. The inset shows the particle Reynolds number $Re_p(y) = |\Delta u(y)|D/\nu$. We see that when St_h is larger, $|\Delta u|$ and therefore Re_p are also larger. In the case of $St_h \gtrsim 1$, we also see that the sign of Δu changes around $y/h \approx 0.3$ irrespective of Re_τ. Since particles with $St_h \gtrsim 1$ cannot follow the swirls of outer-layer vortices, they are slower than fluid in the outer layer. On the other hand, when the particles are swept out by the outer-layer vortices and move into the slower inner layer, the particles become faster than the fluid. Thus, the relative velocity behaves in a qualitatively different manner between the inner and outer layers. In § 4.2, we have defined the outer layer as $y/h \geqslant 0.3$, where Δu depends weakly on y and $\Delta u > 0$.

REFERENCES

ABDELSAMIE, A.H. & LEE, C. 2012 Decaying versus stationary turbulence in particle-laden isotropic turbulence: turbulence modulation mechanism. *Phys. Fluids* **24** (1), 015106.

ARDEKANI, M.N. & BRANDT, L. 2019 Turbulence modulation in channel flow of finite-size spheroidal particles. *J. Fluid Mech.* **859**, 887–901.

ARDEKANI, M.N., COSTA, P., BREUGEM, W.-P., PICANO, F. & BRANDT, L. 2017 Drag reduction in turbulent channel flow laden with finite-size oblate spheroids. *J. Fluid Mech.* **816**, 43–70.

AWAI, H., MOTOORI, Y. & GOTO, S. 2025 Attenuation of turbulence in a periodic cube by anisotropic solid particles. *J. Fluid Mech.* **1008**, A6.

BALACHANDAR, S. 2009 A scaling analysis for point-particle approaches to turbulent multiphase flows. *Intl J. Multiphase Flow* **35** (9), 801–810.

BALACHANDAR, S. & EATON, J.K. 2010 Turbulent dispersed multiphase flow. *Annu. Rev. Fluid Mech.* **42** (1), 111–133.

BALACHANDAR, S., PENG, C. & WANG, L.P. 2024 Turbulence modulation by suspended finite-sized particles: toward physics-based multiphase subgrid modeling. *Phys. Rev. Fluids* **9** (4), 044304.

BELLANI, G., BYRON, M.L., COLLIGNON, A.G., MEYER, C.R. & VARIANO, E.A. 2012 Shape effects on turbulent modulation by large nearly neutrally buoyant particles. *J. Fluid Mech.* **712**, 41–60.

BERNARDINI, M. 2014 Reynolds number scaling of inertial particle statistics in turbulent channel flows. *J. Fluid Mech.* **758**, R1.

BRANDT, L. & COLETTI, F. 2022 Particle-laden turbulence: progress and perspectives. *Annu. Rev. Fluid Mech.* **54** (1), 159–189.

BREUGEM, W.P. 2012 A second-order accurate immersed boundary method for fully resolved simulations of particle-laden flows. *J. Comput. Phys.* **231** (13), 4469–4498.

BURTON, T.M. & EATON, J.K. 2005 Fully resolved simulations of particle-turbulence interaction. *J. Fluid Mech.* **545**, 67–111.

TEN CATE, A., DERKSEN, J.J., PORTELA, L.M. & VAN DEN AKKER, H.E. 2004 Fully resolved simulations of colliding monodisperse spheres in forced isotropic turbulence. *J. Fluid Mech.* **519**, 233–271.

COSTA, P., BRANDT, L. & PICANO, F. 2020 Interface-resolved simulations of small inertial particles in turbulent channel flow. *J. Fluid Mech.* **883**, A54.

COSTA, P., BRANDT, L. & PICANO, F. 2021 Near-wall turbulence modulation by small inertial particles. *J. Fluid Mech.* **922**, A9.

DAVE, H. & KASBAOUI, M.H. 2023 Mechanisms of drag reduction by semidilute inertial particles in turbulent channel flow. *Phys. Rev. Fluids* **8** (8), 084305.

DRITSELIS, C.D. & VLACHOS, N.S. 2008 Numerical study of educed coherent structures in the near-wall region of a particle-laden channel flow. *Phys. Fluids* **20** (5), 055103.

DRITSELIS, C.D. & VLACHOS, N.S. 2011 Numerical investigation of momentum exchange between particles and coherent structures in low Re turbulent channel flow. *Phys. Fluids* **23** (2), 025103.

ELGHOBASHI, S. 1994 On predicting particle-laden turbulent flows. *Appl. Sci. Res.* **52** (4), 309–329.

FERRANTE, A. & ELGHOBASHI, S. 2003 On the physical mechanisms of two-way coupling in particle-laden isotropic turbulence. *Phys. Fluids* **15** (2), 315–329.

FESSLER, J.R. & EATON, J.K. 1999 Turbulence modification by particles in a backward-facing step flow. *J. Fluid Mech.* **394**, 97–117.

FORNARI, W., FORMENTI, A., PICANO, F. & BRANDT, L. 2016 The effect of particle density in turbulent channel flow laden with finite size particles in semi-dilute conditions. *Phys. Fluids* **28** (3), 033301.

GLOWINSKI, R., PAN, T.-W., HESLA, T.I., JOSEPH, D.D. & PERIAUX, J. 2001 A fictitious domain approach to the direct numerical simulation of incompressible viscous flow past moving rigid bodies: application to particulate flow. *J. Comput. Phys.* **169** (2), 363–426.

GORE, R.A. & CROWE, C.T. 1989 Effect of particle size on modulating turbulent intensity. *Intl J. Multiphase Flow* **15** (2), 279–285.

HOSOKAWA, S. & TOMIYAMA, A. 2004 Turbulence modification in gas-liquid and solid-liquid dispersed two-phase pipe flows. *Intl J. Heat Fluids Flow* **25** (3), 489–498.

HWANG, W. & EATON, J.K. 2006 Homogeneous and isotropic turbulence modulation by small heavy ($St \sim 50$) particles. *J. Fluid Mech.* **564**, 361–393.

KAJISHIMA, T., TAKIGUCHI, S., HAMASAKI, H. & MIYAKE, Y. 2001 Turbulence structure of particle-laden flow in a vertical plane channel due to vortex shedding. *JSME Intl J. Ser. B* **44** (4), 526–535.

KIDANEMARIAM, A.G., CHAN-BRAUN, C., DOYCHEV, T. & UHLMANN, M. 2013 Direct numerical simulation of horizontal open channel flow with finite-size, heavy particles at low solid volume fraction. *New J. Phys.* **15** (2), 025031.

KULICK, J.D., FESSLER, J.R. & EATON, J.K. 1994 Particle response and turbulence modification in fully developed channel flow. *J. Fluid Mech.* **277**, 109–134.

KUSSIN, J. & SOMMERFELD, M. 2002 Experimental studies on particle behaviour and turbulence modification in horizontal channel flow with different wall roughness. *Exp. Fluids* **33** (1), 143–159.

LEE, J., AHN, J. & SUNG, H.J. 2015 Comparison of large- and very-large-scale motions in turbulent pipe and channel flows. *Phys. Fluids* **27** (2), 025101.

LI, D., LUO, K. & FAN, J. 2016 Modulation of turbulence by dispersed solid particles in a spatially developing flat-plate boundary layer. *J. Fluid Mech.* **802**, 359–394.

LIU, C., TANG, S., SHEN, L. & DONG, Y. 2017 Characteristics of turbulence transport for momentum and heat in particle-laden turbulent vertical channel flows. *Acta Mechanica Sinica/Lixue Xuebao* **33** (5), 833–845.

LOZANO-DURÁN, A., FLORES, O. & JIMÉNEZ, J. 2012 The three-dimensional structure of momentum transfer in turbulent channels. *J. Fluid Mech.* **694**, 100–130.

LUCCI, F., FERRANTE, A. & ELGHOBASHI, S. 2010 Modulation of isotropic turbulence by particles of Taylor length-scale size. *J. Fluid Mech.* **650**, 5–55.

MAEDA, M., HISHIDA, K. & FURUTANI, T. 1980 Velocity distributions of air-solids suspension in upward pipe flow: effect of particles on air velocity distribution. *JSME Ser. B (in Japanese)* **46** (412), 2313–2320.

MANDØ, M., LIGHTSTONE, M.F., ROSENDAHL, L., YIN, C. & SØRENSEN, H. 2009 Turbulence modulation in dilute particle-laden flow. *Intl J. Heat Fluid Flow* **30** (2), 331–338.

MORTIMER, L.F., NJOBUENWU, D.O. & FAIRWEATHER, M. 2019 Near-wall dynamics of inertial particles in dilute turbulent channel flows. *Phys. Fluids* **31** (6), 063302.

MOTOORI, Y. & GOTO, S. 2019 Generation mechanism of a hierarchy of vortices in a turbulent boundary layer. *J. Fluid Mech.* **865**, 1085–1109.

MOTOORI, Y. & GOTO, S. 2021 Hierarchy of coherent structures and real-space energy transfer in turbulent channel flow. *J. Fluid Mech.* **911**, A27.

MOTOORI, Y., WONG, C. & GOTO, S. 2022 Role of the hierarchy of coherent structures in the transport of heavy small particles in turbulent channel flow. *J. Fluid Mech.* **942**, A3.

MOTOORI, Y. & GOTO, S. 2025 Enhancement of wall-bounded turbulence by solid particles under gravity. *Intl J. Heat Fluid Flow* **116**, 109933.

MURAMULLA, P., TYAGI, A., GOSWAMI, P.S. & KUMARAN, V. 2020 Disruption of turbulence due to particle loading in a dilute gas-particle suspension. *J. Fluid Mech.* **889**, A28.

NOGUCHI, K. & NEZU, I. 2009 Particle–turbulence interaction and local particle concentration in sediment-laden open-channel flows. *J. Hydro-Environ. Res.* **3** (2), 54–68.

OKA, S. & GOTO, S. 2021 Generalized sweep-stick mechanism of inertial-particle clustering in turbulence. *Phys. Rev. Fluids* **6** (4), 044605.

OKA, S. & GOTO, S. 2022 Attenuation of turbulence in a periodic cube by finite-size spherical solid particles. *J. Fluid Mech.* **949**, A45.

PARIS, A.D. 2001 *Turbulence Attenuation in a Particle-Laden Channel Flow*. Stanford University.

PENG, C., AYALA, O.M. & WANG, L.P. 2019*a* A direct numerical investigation of two-way interactions in a particle-laden turbulent channel flow. *J. Fluid Mech.* **875**, 1096–1144.

PENG, C., AYALA, O.M. & WANG, L.P. 2019*b* Flow modulation by a few fixed spherical particles in a turbulent channel flow. *J. Fluid Mech.* **884**, A15.

PENG, C., SUN, Q. & WANG, L.P. 2023 Parameterization of turbulence modulation by finite-size solid particles in forced homogeneous isotropic turbulence. *J. Fluid Mech.* **963**, A6.

PICANO, F., BREUGEM, W.P. & BRANDT, L. 2015 Turbulent channel flow of dense suspensions of neutrally buoyant spheres. *J. Fluid Mech.* **764**, 463–487.

RIGHETTI, M. & ROMANO, G.P. 2004 Particle-fluid interactions in a plane near-wall turbulent flow. *J. Fluid Mech.* **505**, 93–121.

ROGERS, C.B. & EATON, J.K. 1991 The effect of small particles on fluid turbulence in a flat-plate, turbulent boundary layer in air. *Phys. Fluids A* **3** (5), 928–937.

SCHILLER, L. 1933 A drag coefficient correlation. *Zeit. Ver. Deutsch. Ing.* **77**, 318–320.

SCHNEIDERS, L., MEINKE, M. & SCHRÖDER, W. 2017 Direct particle–fluid simulation of Kolmogorov-length-scale size particles in decaying isotropic turbulence. *J. Fluid Mech.* **819**, 188–227.

SHAO, X., WU, T. & YU, Z. 2012 Fully resolved numerical simulation of particle-laden turbulent flow in a horizontal channel at a low Reynolds number. *J. Fluid Mech.* **693**, 319–344.

SHEN, J., PENG, C., LU, Z. & WANG, L.P. 2024 The influence of particle density and diameter on the interactions between the finite-size particles and the turbulent channel flow. *Intl J. Multiphase Flow* **170**, 104659.

SHEN, J., PENG, C., WU, J., CHONG, K.L., LU, Z. & WANG, L.P. 2022 Turbulence modulation by finite-size particles of different diameters and particle-fluid density ratios in homogeneous isotropic turbulence. *J. Turbul.* **23** (8), 433–453.

SOLDATI, A. & MARCHIOLI, C. 2009 Physics and modelling of turbulent particle deposition and entrainment: review of a systematic study. *Intl J. Multiphase Flow* **35** (9), 827–839.

SQUIRES, K.D. & EATON, J.K. 1990 Particle response and turbulence modification in isotropic turbulence. *Phys. Fluids A* **2** (7), 1191–1203.

SUN, Q., PENG, C., WANG, L.P., CHEN, S. & ZHU, Z. 2024 Decay rate of homogeneous isotropic turbulence laden with finite-size particles. *J. Fluid Mech.* **993**, A15.

TANAKA, T. & EATON, J.K. 2008 Classification of turbulence modification by dispersed spheres using a novel dimensionless number. *Phys. Rev. Lett.* **101** (11), 114502.

TAYLOR, G.I. 1935 Statistical theory of turbulence iv-diffusion in a turbulent air stream. *Proc. R. Soc. Lond.* **151** (873), 465–478.

TSUJI, Y. & MORIKAWA, Y. 1982 LDV measurements of an air-solid two-phase flow in a horizontal pipe. *J. Fluid Mech.* **120**, 385–409.

TSUJI, Y., MORIKAWA, Y. & SHIOMI, H. 1984 LDV measurements of an air-solid two-phase flow in a vertical pipe. *J. Fluid Mech.* **139**, 417–434.

UHLMANN, M. 2005 An immersed boundary method with direct forcing for the simulation of particulate flows. *J. Comput. Phys.* **209** (2), 448–476.

UHLMANN, M. 2008 Interface-resolved direct numerical simulation of vertical particulate channel flow in the turbulent regime. *Phys. Fluids* **20** (5), 053305.

UHLMANN, M. & CHOUIPPE, A. 2017 Clustering and preferential concentration of finite-size particles in forced homogeneous-isotropic turbulence. *J. Fluid Mech.* **812**, 991–1023.

VREMAN, A.W. 2007 Turbulence characteristics of particle-laden pipe flow. *J. Fluid Mech.* **584**, 235–279.

WANG, G. & RICHTER, D.H. 2019 Two mechanisms of modulation of very-large-scale motions by inertial particles in open channel flow. *J. Fluid Mech.* **868**, 538–559.

WANG, L.P., AYALA, O., GAO, H., ANDERSEN, C. & MATHEWS, K.L. 2014 Study of forced turbulence and its modulation by finite-size solid particles using the lattice Boltzmann approach. *Comput. Maths Applics.* **67** (2), 363–380.

XIA, Y., LIN, Z., PAN, D. & YU, Z. 2021 Turbulence modulation by finite-size heavy particles in a downward turbulent channel flow. *Phys. Fluids* **33** (6), 063321.

XIA, Y., YU, Z., LIN, Z. & GUO, Y. 2022 Model of interfacial term in turbulent kinetic energy equation and computation of dissipation rate for particle-laden flows. *Phys. Fluids* **34** (8), 083311.

YANG, T.S. & SHY, S.S. 2005 Two-way interaction between solid particles and homogeneous air turbulence: particle settling rate and turbulence modification measurements. *J. Fluid Mech.* **526**, 171–216.

YEO, K., DONG, S., CLIMENT, E. & MAXEY, M.R. 2010 Modulation of homogeneous turbulence seeded with finite size bubbles or particles. *Intl J. Multiphase Flow* **36** (3), 221–233.

YU, Z., LIN, Z., SHAO, X. & WANG, L.P. 2017 Effects of particle-fluid density ratio on the interactions between the turbulent channel flow and finite-size particles. *Phys. Rev. E* **96** (3), 033102.

YU, Z., XIA, Y., GUO, Y. & LIN, J. 2021 Modulation of turbulence intensity by heavy finite-size particles in upward channel flow. *J. Fluid Mech.* **913**, A3.

ZENG, L., BALACHANDAR, S., FISCHER, P. & NAJJAR, F. 2008 Interactions of a stationary finite-sized particle with wall turbulence. *J. Fluid Mech.* **594**, 271–305.

ZHAO, L., ANDERSSON, H.I. & GILLISSEN, J.J. 2013 Interphasial energy transfer and particle dissipation in particle-laden wall turbulence. *J. Fluid Mech.* **715**, 32–59.

ZHAO, L.H., ANDERSSON, H.I. & GILLISSEN, J.J. 2010 Turbulence modulation and drag reduction by spherical particles. *Phys. Fluids* **22** (8), 081702.

ZHOU, T., ZHAO, L., HUANG, W. & XU, C. 2020 Non-monotonic effect of mass loading on turbulence modulations in particle-laden channel flow. *Phys. Fluids* **32** (4), 043304.